MOX–Report No. 15/2012

A comparative study of different nonlinear hyperelastic isotropic arterial wall models in patient-specific vascular flow simulations in the aortic arch

Mengaldo, G.; Tricerri, P.; Crosetto,P.; Deparis, S.; Nobile, F.; Formaggia, L.

MOX, Dipartimento di Matematica "F. Brioschi"
Politecnico di Milano, Via Bonardi 9 - 20133 Milano (Italy)

mox@mate.polimi.it http://mox.polimi.it

A COMPARATIVE STUDY OF DIFFERENT NONLINEAR HYPERELASTIC ISOTROPIC ARTERIAL WALL MODELS IN PATIENT-SPECIFIC VASCULAR FLOW SIMULATIONS IN THE AORTIC ARCH *

Gianmarco Mengaldo[1], Paolo Tricerri[2,3], Paolo Crosetto[3], Simone Deparis[3], Fabio Nobile[1,4] and Luca Formaggia[1]

Abstract. Blood flow in major arteries gives rise to a complex fluid-structure interaction (FSI) problem. The mechanical behaviour of the tissues composing the vessel wall is highly nonlinear. However, when the wall deformation is small it can be argued that the effect of the non-linearities to the flow field is small and indeed several authors employ a linear constitutive law. In the aortic arch, however, the deformations experienced by the vessel wall during the heart beat are substantial. In this work we have implemented different non-linear constitutive relations for the vessel wall. We compare the flow field and related quantities such as wall shear stress obtained on an anatomically realistic geometry of aortic arch reconstructed from clinical images and using physiological data. Particular attention is also devoted to the efficiency of the algorithms employed. The fluid-structure interaction problem is solved with a fully coupled approach and using the exact Jacobians for each different structural model to guarantee a second order convergence of the Newton method.

1991 Mathematics Subject Classification. 65M60, 74F10, 65Y05, 65Y20.

March 6, 2012.

1. Introduction

In the recent years we have witnessed a substantial increase of the application of mathematical models and numerical simulations to the study of the vascular system in different physiological and pathological situations, such as aneurysms, thrombosis, atherosclerosis, etc. It is well known that arteries are compliant, and the deformation of the arterial wall may affect the dynamics of blood

Keywords and phrases: arterial wall modelling, patient-specific simulation, fluid-structure interaction, aortic arch

* *We acknowledge the Swiss Platform for High-Performance and High-Productivity Computing (HP2C), the Swiss National Supercomputing Center (CSCS) for the XE6 supercomputer Rosa, Dr. Philippe Reymond and LHTC for the aorta geometry and boundary data. The authors want also to thank Dr. Mariarita Deluca for her help throughout all the work.*

[1] MOX - Dept. of Mathamatics F.Brioschi, Via Bonardi 9, 20133 Milano, Italy;
e-mail: g.mengaldo11@imperial.ac.uk, luca.formaggia@polimi.it
[2] CEMAT-Centro de Matemática e Aplicações, IST, 1000-081 Lisbon, Portugal;
[3] MATHICSE-CMCS, EPFL, CH-1015 Lausanne, Switzerland;
e-mail: paolo.tricerri@epfl.ch, paolo.crosetto@epfl.ch, simone.deparis@epfl.ch
[4] MATHICSE-CSQI, EPFL, CH-1015 Lausanne, Switzerland;
e-mail: fabio.nobile@epfl.ch

flow and the computation of important derived quantities like wall shear stress, particularly in large arteries. Even if the main effects of compliance on the blood flow may be accounted for using simple linear structural models, the actual mechanical behaviour of arterial tissue is far from linear. It is then expected that some important details may be lost if this non-linearity is neglected, especially in major arteries like the aorta, where the vessel deformation during a heart beat is rather large.

This paper focuses on comparing different structural models for the vessel wall when modelling the coupled fluid-structure interaction (FSI) problems that arise in haemodynamics. In particular, the attention is placed on the simulation of the blood flow and arterial wall dynamics in the aortic arch.

When studying such a complex coupled system, the mathematical models for the blood ("the fluid") and the arterial wall ("the structure") should capture the correct mechanical behaviour, which can differ depending on the type of vessel under study [15, 23, 41]. In this work, blood is modelled as a Newtonian fluid. This hypothesis is commonly accepted in literature for flow in main blood vessels (e.g. [4,6,10,11,17,19]) though it may be inaccurate in the small ones, or when the shear stress in the fluid is below a critical threshold (e.g. in the venous system). In both cases blood starts to deviate from the Newtonian properties. However, in this work we focus on the aortic arch, where the assumption of Newtonian fluid is acceptable.

As concerns the arterial wall, it is known that it is composed of three main layers (tunica intima, media and advetitia). The most important feature of the passive (non stimulated) mechanical behaviour of an artery is that the stress-strain relation during loading and unloading is highly nonlinear. Therefore, when a vessel undergoes relatively large deformations it is expected that a reliable constitutive model for the vessel wall can be crucial for the accurate computation of some mechanical factors which are considered important in triggering the onset of a cardiovascular disease (e.g. aneurysms and atherosclerosis), or when investigating the effect of changes of the arterial tissue behaviour due to factors like aging or hypertension.

In the last four decades, several models were proposed to describe the vessel wall dynamics using different theoretical frameworks like finite elasticity or mixture theory. These models are reviewed in detail in [16,32,36]. It is commonly agreed that in young healthy arteries, only the media and adventitia layers are responsible for the mechanical response of the arterial wall. Their contribution to the overall mechanical behaviour of the biological tissue occurs at different levels of strain [14, 42]. In a disease situation the mechanical properties of the wall may differ significantly from those of healthy arteries and, in some cases, the intima layer may become relevant [26]. In this work, four structural models which are commonly used in literature to describe the arterial tissue have been used. Namely, linear elasticity, St.Venant-Kirchhoff, Neo-Hookean and exponential models. They have been developed in the framework of nonlinear finite elasticity [12]. From the mathematical point of view, these models describe the biological tissue as a compressible (the first two) and nearly-incompressible (the second two), isotropic and hyperelastic material. From experimental observations, the arterial tissue is known to be incompressible or near-incompressible. In this work, the volume preserving constraint is enforced in the finite element code (implemented in the finite element library `LifeV` [9]) using high Poisson ratios for the first two models, and by decomposing the constitutive relation into a volumetric and isochoric part for the second two. Particular care needs to be devoted to the choice of Poisson ratio and bulk modulus when getting too close to incompressibility regime, because of the locking phenomenon.

In the following, only preconditioned materials are considered, that is materials where the typical stress softening effect (which occurs during the first few load cycles) is no longer evident. Moreover, we have neglected pre-stress. This is a limitation of the present study since arterial wall exhibit pre-stress, but we feel that the comparison of the results obtained with the different models may give already good indications even in this simplified situation.

It is commonly accepted that haemodynamic induced stresses have an important role in the initiation and progression of arterial pathologies. Several studies have been focused on their evaluation only considering blood flow in idealized and anatomically realistic geometries [3,4,6,20,31,34]. We consider here, instead, a geometry reconstructed from real patient data.

The coupled FSI system is an highly nonlinear problem not only because of the non-linearity in the Navier-Stokes equations and possibly in the constitutive relation to describe the structure, but also because of the geometric non-linearity induced by the relative large displacements. In this work this is handled resorting to an arbitrary Lagrangian Eulerian (ALE) frame of reference. The advantage with respect to the Eulerian description is that the coupling conditions can be satisfied exactly on the fluid-structure interface. However, this approach requires to introduce an additional set of equations to describe the deformation of the fluid domain. In this work the complete system of nonlinear algebraic equations that arises from the discretization of the coupled problem is solved as a whole, using a Newton scheme. In this case, the use of preconditioning techniques and domain decomposition methods plays a key role in obtaining an efficient solution method, particularly in a parallel setting [1, 25].

We have considered the simulation of blood flow in a patient-specific aortic arch using physiological inlet/outlet flow conditions [5,29], realistic material parameters, and the cited four different structural models for the arterial tissue. The goal is to understand how the different mechanical models for the vessel wall influence the distribution of hemodynamic indicators like wall shear stress (WSS) and the displacement field in the structural domain. Different researches have already carried out similar analyses [11, 18, 37–39]). Yet, to the best of our knowledge, no comparisons of the results obtained using three different nonlinear structural models have been carried out so far. Moreover in the cited literature no details are given about the linearization of the first Piola-Kirchhoff tensor. Indeed, when the structure problem has to be linearized, the computations of the Jacobian of the stress tensor is delicate and not straightforward. Considering this, we give here the complete definition of the first Piola-Kirchhoff tensor and of its Jacobian for each of the constitutive laws we have considered.

This paper is divided in four sections. Sect. §2 deals with the mathematical modelling of continuum bodies. It gives a brief introduction on the equations governing the motion of solid bodies and the quantities involved in the problem. In particular, we describe the constitutive relations used in this work and we give the mathematical formulation of the coupled fluid-structure interaction problem. The third section describes the treatment of the nonlinearities of both the solid problem, when using nonlinear constitutive laws, and the FSI problem. The computation of the Jacobian of the Piola-Kichhoff tensor for each material model is detailed. The final part of the section is devoted to illustrate the linearization of the FSI problem adopted for its numerical solution. In Sect. §4 we provide some numerical results. First, the convergence rate of the Newton method applied to two test cases of nonlinear structural and FSI problems are presented. We show that in both cases, the convergence rate corresponds to the theoretical one, verifying the correct implementation of the structural laws. After that, we consider a patient-specific FSI simulation in an aortic arch. The numerical results obtained in this case are shown and critically analyzed. Particular attention has been dedicated to the computation of haemodynamic indicators which are known to be related to the onset of cardiovascular diseases. The final section summarizes the results and draws some conclusions. Besides, it identifies important future directions that would enhance the current state of blood flow simulations.

2. Mathematical Modelling

2.1. **Arterial tissue modelling**

Let $\mathcal{B}_0 \subset \mathbb{R}^3$ an open set with smooth boundary $\partial\mathcal{B}_0$, defining a continuum body (the arterial wall). We refer to $\mathcal{B}_0$ as the reference configuration of the vessel wall at the initial time $t_0 = 0$. When the body moves, at each time $t > 0$, it will occupy a new configuration $\mathcal{B}(t)$, namely the current configuration. In the framework of continuum mechanics, the motion of the vessel wall in a temporal interval of interest $[0, T]$, is described by a map $\chi : \overline{\mathcal{B}_0} \times [0, T] \to \mathbb{R}^3$, where $\overline{\mathcal{B}_0}$ is the closure of $\mathcal{B}_0$. This map transforms a material point $\boldsymbol{X} \in \mathcal{B}_0$ into a point $\boldsymbol{x} = \chi(\boldsymbol{X}, t) \in \mathcal{B}(t)$ at any time $t > 0$.
The Lagrangian description of the kinematics quantities of the motion (e.g. displacement and velocity fields) is obtained via the map χ. The displacement field is defined as $\widehat{\boldsymbol{\eta}}(\boldsymbol{X}, t) = \boldsymbol{x}(\boldsymbol{X}, t) - \boldsymbol{X}$ and the velocity field is $\widehat{\boldsymbol{v}}(\boldsymbol{X}, t) = \dfrac{\partial}{\partial t}\widehat{\boldsymbol{\eta}}(\boldsymbol{X}, t)$. The gradient of χ with respect to the material coordinates $\boldsymbol{X}$ is called the deformation gradient tensor $\mathbf{F}$ and it is useful for defining other tensors such as the right Cauchy-Green and the Green-Lagrange tensors.
The Lagrangian form of the equation of motion to describe the structural dynamics problem is:

$$\rho_s \frac{\partial^2 \widehat{\boldsymbol{\eta}}}{\partial t^2} = \rho_s \boldsymbol{b} + \mathrm{Div}(\mathbf{P}) \qquad \forall \boldsymbol{X} \subseteq \mathcal{B}_0 \times (0, T], \tag{1}$$

where the divergence Div is taken with respect to the material coordinates $\boldsymbol{X}$, ρ_s is the density of the arterial tissue, $\boldsymbol{b}$ represents the volume forces and $\mathbf{P}$ is the first Piola-Kirchhoff tensor, which is related to the Cauchy stress tensor σ by $\mathbf{P} = J\sigma\mathbf{F}^{-T}$, where $J = \det(\mathbf{F})$. When initial and boundary conditions are added to Eq. (1) the mathematical problem associated to Eq. (1) is defined. In order to make it solvable, a constitutive relation that describes the Cauchy stress tensor as a function of the deformation gradient tensor $\mathbf{F}$ is needed. In this work, Cauchy elastic, homogeneous and hyperelastic materials are taken into account. The incompressibility constraint which the biological tissue obeys is enforced in the models via the first Lamé coefficient and the shear modulus in the linear elasticity and in the St.Venant-Kirchhoff law, and by decomposing the constitutive relation into the sum of an isochoric and volumetric terms in the Neo-Hookean and exponential models [27]. In the following subsections, the computations to derive the first Piola-Kirchhoff tensor from the strain energy function $\mathcal{W}$ are not shown. The interested reader may refer to [13, 21, 33] and references therein.

2.1.1. *St. Venant-Kirchhoff constitutive law*

St.Venant-Kirchhoff constitutive law is described by the following form of the strain energy function $\mathcal{W}$:

$$\mathcal{W}(\mathbf{E}) = \frac{\lambda}{2}(\mathrm{tr}\mathbf{E})^2 + \mu\mathbf{E} : \mathbf{E}, \tag{2}$$

where $\mathbf{E}$ is the Green-Lagrange tensor and it is defined as $\mathbf{E} = \frac{1}{2}\left(\mathbf{F}^T\mathbf{F} - \mathbf{I}\right)$, and λ and μ are the first Lamé constant and the shear modulus respectively. Without loss of generality, the strain energy function can be expressed as a function of the invariants $\left(I_{\mathbf{C}}, II_{\mathbf{C}}, III_{\mathbf{C}}\right)$ of the right Cauchy-Green tensor ($\mathbf{C}$),

$$\mathcal{W} = \left(\frac{\lambda}{8} + \frac{\mu}{4}\right) I_{\mathbf{C}}^2 - \left(\frac{3\lambda}{4} + \frac{\mu}{2}\right) I_{\mathbf{C}} - \frac{\mu}{2} II_{\mathbf{C}} + \frac{9\lambda}{8} + \frac{3\mu}{4}. \tag{3}$$

The first Piola-Kirchhoff tensor, as a function of the deformations, in the case of St. Venant-Kirchhoff model reads:

$$\mathbf{P} = \frac{\lambda}{2}\big(I_{\mathbf{C}} - 3\big)\mathbf{F} + \mu\mathbf{F} + \mu\mathbf{F}\mathbf{C}. \tag{4}$$

If the displacement field is introduced in Eq. (4), the definition of $\mathbf{P}$ becomes:

$$\begin{aligned}\mathbf{P}(\widehat{\boldsymbol{\eta}}) = \quad & \lambda(\mathrm{Div}\big(\widehat{\boldsymbol{\eta}}\big))\mathbf{I} + \mu\big(\widehat{\boldsymbol{\nabla}}\widehat{\boldsymbol{\eta}} + \widehat{\boldsymbol{\nabla}}\widehat{\boldsymbol{\eta}}^T\big) + \frac{\lambda}{2}\big(\widehat{\boldsymbol{\nabla}}\widehat{\boldsymbol{\eta}} : \widehat{\boldsymbol{\nabla}}\widehat{\boldsymbol{\eta}}\big) + \\ & + \lambda\big(\mathrm{Div}\big(\widehat{\boldsymbol{\eta}}\big)\big)\widehat{\boldsymbol{\nabla}}\widehat{\boldsymbol{\eta}} + \frac{\lambda}{2}\big(\widehat{\boldsymbol{\nabla}}\widehat{\boldsymbol{\eta}} : \widehat{\boldsymbol{\nabla}}\widehat{\boldsymbol{\eta}}\big)\widehat{\boldsymbol{\nabla}}\widehat{\boldsymbol{\eta}} + \mu\big(\widehat{\boldsymbol{\nabla}}\widehat{\boldsymbol{\eta}}^T\widehat{\boldsymbol{\nabla}}\widehat{\boldsymbol{\eta}}\big) + \\ & + \mu\widehat{\boldsymbol{\nabla}}\widehat{\boldsymbol{\eta}}\big(\widehat{\boldsymbol{\nabla}}\widehat{\boldsymbol{\eta}}\widehat{\boldsymbol{\nabla}}\widehat{\boldsymbol{\eta}}^T\big) + \mu\widehat{\boldsymbol{\nabla}}\widehat{\boldsymbol{\eta}}\widehat{\boldsymbol{\nabla}}\widehat{\boldsymbol{\eta}}^T\widehat{\boldsymbol{\nabla}}\widehat{\boldsymbol{\eta}}.\end{aligned} \tag{5}$$

Linear elasticity can be deduced from Eq. (5) by considering only the linear terms, obtaining

$$\mathbf{P}(\widehat{\boldsymbol{\eta}}) = \lambda(\mathrm{Div}\big(\widehat{\boldsymbol{\eta}}\big))\mathbf{I} + \mu\big(\widehat{\boldsymbol{\nabla}}\widehat{\boldsymbol{\eta}} + \widehat{\boldsymbol{\nabla}}\widehat{\boldsymbol{\eta}}^T\big). \tag{6}$$

It is worth to remind that the St. Venant-Kirchhoff strain energy function Eq. (2) may not be recommended in case of large compressive strains which might occur in regions of arterial branching. In fact, it does not satisfy the policonvexity condition (which is a sufficient condition on $\mathcal{W}$ for the well posedness of the structural problem) for such states of deformation (see [2]). Despite this limitation, the St.Venant-Kirchhoff model is commonly used in the literature to describe the arterial wall.

2.1.2. *Neo-Hookean constitutive law*

In the case of Neo-Hookean law we use the multiplicative decomposition of $\mathbf{F}$,

$$\mathbf{F} = \widehat{\mathbf{F}}\bar{\mathbf{F}}, \tag{7}$$

where $\widehat{\mathbf{F}}$ is the volumetric part and $\bar{\mathbf{F}}$ is the isochoric term (see [27]). This results in splitting the strain energy function as follows:

$$\mathcal{W} = \frac{\mu}{2}\big(I_{\bar{\mathbf{C}}} - 3\big) + \frac{\kappa}{4}\left[(J-1)^2 + (\ln J)^2\right], \tag{8}$$

where μ is the shear modulus and κ is the bulk modulus. The higher the bulk modulus the more incompressible the material behaves. The first term in Eq. (10) is the isochoric contribution and the second represents the volumetric term of $\mathcal{W}$. The tensor $\mathbf{P}$ is:

$$\mathbf{P} = \mu J^{-\frac{2}{3}}\left(\mathbf{F} - \frac{1}{3}I_{\bar{\mathbf{C}}}\mathbf{F}^{-T}\right) + J\frac{\kappa}{2}\left(J - 1 + \frac{1}{J}\ln J\right)\mathbf{F}^{-T}. \tag{9}$$

For this class of materials, the policonvexity condition is satisfied for all the states of deformation. Hence, the mathematical structural dynamics problem generated by Eq. (1) is well posed.

2.1.3. *Exponential constitutive law*

Again in this case, the definition (7) is used, and the exponential strain energy function $\mathcal{W}$ reads:

$$\mathcal{W} = \frac{\alpha}{2\gamma}\left(e^{\gamma(\mathbf{I}_{\bar{\mathbf{C}}}-3)} - 1\right) + \frac{\kappa}{4}\left[(J-1)^2 + (\ln J)^2\right], \tag{10}$$

where α and γ are material parameters and κ is, as in Sect. §2.1.2, the bulk modulus. The tensor $\mathbf{P}$ reads:

$$\mathbf{P} = \alpha J^{-\frac{2}{3}} \left(\mathbf{F} - \frac{1}{3} I_{\bar{\mathbf{C}}} \mathbf{F}^{-T} \right) e^{\gamma \left(I_{\bar{\mathbf{C}}} - 3 \right)} + J \frac{\kappa}{2} \left(J - 1 + \frac{1}{J} \ln J \right) \mathbf{F}^{-T}. \tag{11}$$

As before, the first term in Eq. (11) is the isochoric part of the constitutive laws and the second term enforces the volume preserving constraint. As for the Neo-Hookean law, the policonvexity condition is satisfied for all the states of deformation leading to the well posedness of the mathematical problem related to Eq. (1).

2.2. **Fluid-Structure Interaction modelling**

The domain under consideration is composed by a fluid and a compliant vessel wall (see Fig. 1). In Fig. 1, $\mathcal{F}_0$, $\mathcal{B}_0$ and Γ^0 are the fluid, structure and interface reference configurations respectively.

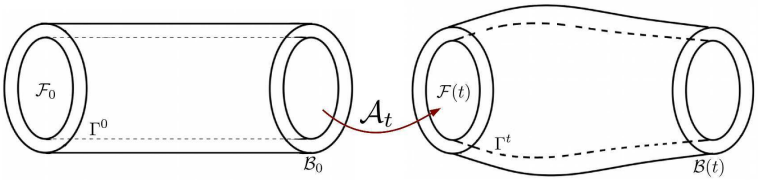

FIGURE 1. FSI domain. On the left, the reference configuration. On the right, the current configuration.

Their corresponding current configurations are indicated by $\mathcal{F}(t)$, $\mathcal{B}(t)$ and Γ^t.

The mathematical model for the coupled system is described by the Navier-Stokes equations for the fluid and by the elasticity equation for the structure, Eq. (1), with the different definitions of $\mathbf{P}$ (Eqs. (5), (6), (9), (11)) described above. The fluid flow is assumed to be laminar Newtonian and incompressible. The governing equations for the fluid problem are formulated in the ALE frame of reference which makes them suitable for fluid-structure problems with frequent mesh adjustments. As said in Sect. §2, this choice yields to a further equation for the fluid domain displacement. Different techniques are available to describe the movement of the fluid domain $\mathcal{F}_0$ (see [35]); in this paper, the harmonic extension of the interface displacement is chosen. Given the displacement of the interface Γ^0, $\boldsymbol{\eta}_f|_{\Gamma^0}$, the displacement field of the fluid domain is described by the differential problem:

$$\begin{cases} -\Delta \boldsymbol{\eta}_f = 0 & \text{in } \mathcal{F}_0 \\ \\ \boldsymbol{\eta}_f = \boldsymbol{\eta}_f|_{\Gamma^0} & \text{on } \Gamma^0. \end{cases} \tag{12}$$

Then, the ALE map $\mathcal{A}$ is defined as:

$$\mathcal{A} \quad : \quad \mathcal{F}_0 \to \mathcal{F}(t) : \qquad \boldsymbol{X} \mapsto \mathcal{A}(\boldsymbol{X}) = \boldsymbol{X} + \boldsymbol{\eta}_f(\boldsymbol{X}), \tag{13}$$

where, now $\boldsymbol{X}$ is a material point in the fluid domain. The velocity of the fluid domain $\boldsymbol{u}_g$ is provided by

$$\boldsymbol{u}_g = \frac{\partial \mathcal{A}}{\partial t}\Big|_{\boldsymbol{X}} = \frac{\partial \boldsymbol{\eta}_f}{\partial t}\Big|_{\boldsymbol{X}}, \tag{14}$$

and the ALE form of the Navier-Stokes equations is then given as

$$\begin{cases} \rho_f \dfrac{\partial \boldsymbol{u}_f}{\partial t}\Big|_{\boldsymbol{X}} + (\rho_f(\boldsymbol{u}_f - \boldsymbol{u}_g)\cdot\nabla)\boldsymbol{u}_f - \mathrm{div}(\sigma_f) = 0 & \text{in } \mathcal{F}(t)\times[0,T] \\ \mathrm{div}(\boldsymbol{u}_f) = 0 & \text{in } \mathcal{F}(t)\times[0,T], \end{cases} \tag{15}$$

where ρ_f is the density of the fluid, $\nabla(\cdot)$ and $\mathrm{div}(\cdot)$ are the gradient and divergence operators in the spatial coordinates in the current configuration of the fluid domain $\mathcal{F}(t)$, and $\sigma_f = -p\mathbf{I} + \mu_f(\nabla\boldsymbol{u}_f + \nabla\boldsymbol{u}_f^T)$ is the stress tensor for the Newtonian fluid model and μ_f is the fluid viscosity. The solid model is described by Eq. (1) and closed when the tensor $\mathbf{P}$ is defined by a constitutive relation.

To couple the two subsystems three conditions are imposed on the interface between the fluid and the structure. The first is the continuity of the stresses,

$$\mathbf{P}\boldsymbol{n}^0 = J\sigma_f\mathbf{F}^{-T}\boldsymbol{n}^0 \qquad \text{on } \Gamma^0, \tag{16}$$

where $\boldsymbol{n}^0$ is the outward normal vector to the fluid (or to the solid) domain and $\mathbf{F}$ is the deformation gradient of the solid domain and J is its determinant. The second is the continuity of the velocities,

$$\boldsymbol{u}_f \circ \mathcal{A} = \frac{d\widehat{\boldsymbol{\eta}}}{dt} \qquad \text{on } \Gamma^0, \tag{17}$$

and the third is geometric adherence, already introduced in Eq. (12),

$$\boldsymbol{\eta}_f = \widehat{\boldsymbol{\eta}} \qquad \text{on } \Gamma^0. \tag{18}$$

Other boundary conditions have to been imposed on the fluid and solid domain. In particular, inflow/outflow boundary conditions are imposed at the artificial boundaries of the fluid domain, homogeneous Dirichlet boundary conditions on the right and left extremities of the structure, and a stress free condition on the external surface of the vessel wall. The initial conditions for the coupled problem will be specified later on.

3. Treatment of the nonlinearities

3.1. Numerical approach to the coupled problem

As pointed out in the previous section, the FSI problem is highly nonlinear. The nonlinearities are due both to the mechanical models for the fluid and structure and to the ALE formulation of the Navier-Stokes equations. When the FSI differential problem is discretized in space and time, a nonlinear algebraic system has to be solved at each time step. In particular, the FSI problem is discretized in space using the Finite Element Method (FEM) and using Backward Difference Formulas (BDF) in time. The derivation of the continuous and discrete weak formulations is not addressed here for sake of brevity (see [25]). Hereafter, the notation used in [1] is adopted to write Eqs. (1)-(15)-(12) in a compact form; the equations have to be understood in the sense of distributions. The fluid problem with interface condition (17) will be represented by the operator F, i.e.:

$$\mathsf{F}(\boldsymbol{u}_f, \widehat{\boldsymbol{\eta}}, \boldsymbol{\eta}_f) = 0, \tag{19}$$

where the arguments of the operator are the fluid velocity, and structural and fluid domain displacement respectively.

The solid problem with the coupling conditions Eq. (16) will be indicated by

$$\mathsf{S}(\boldsymbol{u}_f, \widehat{\boldsymbol{\eta}}) = 0, \tag{20}$$

and the geometric problem with the geometric adherence condition (Eq. (18)) reads

$$\mathsf{G}(\widehat{\boldsymbol{\eta}}, \boldsymbol{\eta}_f) = 0. \tag{21}$$

The FSI system can be synthetically represented as follows:

$$\begin{cases} \mathsf{F}(\boldsymbol{u}_f, \widehat{\boldsymbol{\eta}}, \boldsymbol{\eta}_f) & = 0, \\ \mathsf{S}(\boldsymbol{u}_f, \widehat{\boldsymbol{\eta}}) & = 0, \\ \mathsf{G}(\widehat{\boldsymbol{\eta}}, \boldsymbol{\eta}_f) & = 0. \end{cases} \tag{22}$$

As pointed out in [1,25], different techniques to treat the three nonlinearities of the FSI problem are available. According to the chosen time discretization of the nonlinear terms in Eqs. (1)-(15)-(12), different algebraic systems (linear or nonlinear) can be obtained. In the present work, the so-called fully implicit discretization is adopted. According to this technique, all the terms of the equations are considered implicitly, givin rise to a highly nonlinear system, whose linearization is obtained using a Newton method. In the next subsections the linearization of the constitutive laws presented in Sect. §2 and that of the whole FSI nonlinear system are shown. From now on, only the discretized problems are considered, and the discrete unknowns of the problems are indicated using the same notations as above but omitting their dependence on the grid size (h) and time step (Δt).

3.2. **Linearization of the structural problem**

When the structure problem is discretized in space and time, assuming the structural displacement field is known at a certain time $t = t^n$, the general form of the nonlinear algebraic system reads:

$$\xi \mathbf{M} \widehat{\boldsymbol{\eta}}^{n+1} + \underline{K}_{\mathsf{S}}(\widehat{\boldsymbol{\eta}}^{n+1}) = \underline{G}\left(\mathbf{f}^{n+1}, \widehat{\boldsymbol{\eta}}^{n}, \widehat{\boldsymbol{w}}^{n}, \widehat{\boldsymbol{a}}^{n}\right), \tag{23}$$

where ξ is related to the time marching procedure, $\mathbf{M}$ is the mass matrix, $\underline{K}_{\mathsf{S}}(\widehat{\boldsymbol{\eta}}^{n+1})$ is the stiffness term related to the first Piola-Kirchhoff tensor, and $\underline{G}$ is a function of the forcing terms, structural displacement, velocity and acceleration fields at the previous time. Let us define the operator $\mathsf{L} : \mathbb{R}^{N_h} \to \mathbb{R}^{N_h}$:

$$\widehat{\boldsymbol{\eta}}^{n+1} \mapsto \mathsf{L}(\widehat{\boldsymbol{\eta}}^{n+1}) = \xi \mathbf{M} \widehat{\boldsymbol{\eta}}^{n+1} + \underline{K}_{\mathsf{S}}(\widehat{\boldsymbol{\eta}}^{n+1}) - \underline{G}\left(\mathbf{f}^{n+1}, \widehat{\boldsymbol{\eta}}^{n}, \widehat{\boldsymbol{w}}^{n}, \widehat{\boldsymbol{a}}^{n}\right), \tag{24}$$

where N_h is the dimension of the unknown vectors according to the space discretization. The application of the Newton method implies the computation of the Jacobian matrix of L. Considering that the mass matrix is constant and the function $\underline{G}$ does not depend on the current solution, only the computation of the Jacobian of the stiffness term is needed. We give hereafter the expressions for the Jacobian matrices for the 3 models considered. Details on the derivation can be found in [21]. In the

case of the St. Venant-Kirchhoff model, the Fréchet derivative of the tensor $\mathbf{P}$ (Eq. (5)) reads:

$$
\begin{aligned}
D_{\widehat{\boldsymbol{\eta}}}\mathrm{K_S}(\widehat{\boldsymbol{\eta}}) \quad &= \lambda(\mathrm{Div}\big(\delta\widehat{\boldsymbol{\eta}}\big))\mathbf{I} + \mu(\widehat{\boldsymbol{\nabla}}(\delta\widehat{\boldsymbol{\eta}}) + \widehat{\boldsymbol{\nabla}}(\widehat{\boldsymbol{\eta}})^T) + \\
&+\lambda\widehat{\boldsymbol{\nabla}}\widehat{\boldsymbol{\eta}} : \widehat{\boldsymbol{\nabla}}(\delta\widehat{\boldsymbol{\eta}}) + \lambda(\mathrm{div}\widehat{\boldsymbol{\eta}})\widehat{\boldsymbol{\nabla}}(\delta\widehat{\boldsymbol{\eta}}) + \\
&+\lambda(\mathrm{div}(\delta\widehat{\boldsymbol{\eta}})\widehat{\boldsymbol{\nabla}}\widehat{\boldsymbol{\eta}}) + \frac{\lambda}{2}(\widehat{\boldsymbol{\nabla}}(\delta\widehat{\boldsymbol{\eta}}) : \widehat{\boldsymbol{\nabla}}\widehat{\boldsymbol{\eta}})\widehat{\boldsymbol{\nabla}}\widehat{\boldsymbol{\eta}} + \\
&+\frac{\lambda}{2}(\widehat{\boldsymbol{\nabla}}\widehat{\boldsymbol{\eta}} : \widehat{\boldsymbol{\nabla}}(\delta\widehat{\boldsymbol{\eta}}))\widehat{\boldsymbol{\nabla}}\widehat{\boldsymbol{\eta}} + \frac{\lambda}{2}(\widehat{\boldsymbol{\nabla}}\widehat{\boldsymbol{\eta}} : \widehat{\boldsymbol{\nabla}}(\widehat{\boldsymbol{\eta}}))\widehat{\boldsymbol{\nabla}}(\delta\widehat{\boldsymbol{\eta}}) + \\
&+\mu(\widehat{\boldsymbol{\nabla}}\widehat{\boldsymbol{\eta}})^T\widehat{\boldsymbol{\nabla}}(\delta\widehat{\boldsymbol{\eta}}) + \mu(\widehat{\boldsymbol{\nabla}}(\delta\widehat{\boldsymbol{\eta}}))^T(\widehat{\boldsymbol{\nabla}}\widehat{\boldsymbol{\eta}}) + \\
&+\mu(\widehat{\boldsymbol{\nabla}}\widehat{\boldsymbol{\eta}})^T\widehat{\boldsymbol{\nabla}}(\delta\widehat{\boldsymbol{\eta}}) + \mu\widehat{\boldsymbol{\nabla}}(\delta\widehat{\boldsymbol{\eta}})\widehat{\boldsymbol{\nabla}}\widehat{\boldsymbol{\eta}} + \\
&+\mu\widehat{\boldsymbol{\nabla}}\widehat{\boldsymbol{\eta}}(\widehat{\boldsymbol{\nabla}}(\delta\widehat{\boldsymbol{\eta}}))^T + \mu\widehat{\boldsymbol{\nabla}}(\delta\widehat{\boldsymbol{\eta}})(\widehat{\boldsymbol{\nabla}}\widehat{\boldsymbol{\eta}})^T + \\
&+\mu\widehat{\boldsymbol{\nabla}}(\delta\widehat{\boldsymbol{\eta}})(\widehat{\boldsymbol{\nabla}}\widehat{\boldsymbol{\eta}})^T\widehat{\boldsymbol{\nabla}}\widehat{\boldsymbol{\eta}} + \mu\widehat{\boldsymbol{\nabla}}\widehat{\boldsymbol{\eta}}(\widehat{\boldsymbol{\nabla}}(\delta\widehat{\boldsymbol{\eta}}))^T\widehat{\boldsymbol{\nabla}}\widehat{\boldsymbol{\eta}} + \\
&+\mu\widehat{\boldsymbol{\nabla}}\widehat{\boldsymbol{\eta}}(\widehat{\boldsymbol{\nabla}}\widehat{\boldsymbol{\eta}})^T\widehat{\boldsymbol{\nabla}}(\delta\widehat{\boldsymbol{\eta}}).
\end{aligned}
\tag{25}
$$

For the linear elastic model, the first Piola-Kirchhoff tensor is a linear tensorial function of the displacement field and, for this reason, its Jacobian is equal to the tensor itself (Eq. (6)).
The Neo-Hookean and Exponential models do not allow an explicit derivation of the Jacobian of first Piola- Kirchhoff tensor in terms of the displacement due to their dependence on $\mathbf{F}^{-T}$. In these cases the expression of the Jacobian depends directly on $\mathbf{F}$ which depends, on its turn, on $\widehat{\boldsymbol{\eta}}$. The Jacobian matrix of the Neo-Hookean model (Eq. (9)) is:

$$
\begin{aligned}
D_{\widehat{\boldsymbol{\eta}}}\mathrm{K_S}(\mathbf{F}(\widehat{\boldsymbol{\eta}})) = \quad &-\frac{2}{3}\mu\mathrm{J}^{-2/3}(\mathbf{F}^{-\mathrm{T}} : \delta\mathbf{F})\mathbf{F} + \frac{2}{9}\mu\mathrm{I}_1(\overline{\mathbf{C}})(\mathbf{F}^{-\mathrm{T}} : \delta\mathbf{F})\mathbf{F}^{-\mathrm{T}} + \\
&-\frac{2}{3}\mu\mathrm{J}^{2/3}(\mathbf{F} : \delta\mathbf{F})\mathbf{F}^{-\mathrm{T}} + \mu\mathrm{J}^{-2/3}\delta\mathbf{F} + \frac{\mu}{3}\mathrm{I}_1(\overline{\mathbf{C}})\mathbf{F}^{-\mathrm{T}}\delta\mathbf{F}^{\mathrm{T}}\mathbf{F}^{-\mathrm{T}} + \\
&+\frac{\kappa}{2}\mathrm{J}\Big(2\mathrm{J} - 1 + \frac{1}{J}\Big)(\mathbf{F}^{-\mathrm{T}} : \delta\mathbf{F})\mathbf{F}^{-\mathrm{T}} + \\
&-\frac{\kappa}{2}(\mathrm{J}^2 - \mathrm{J} + \mathrm{lnJ})\mathbf{F}^{-\mathrm{T}}\delta\mathbf{F}^{\mathrm{T}}\mathbf{F}^{-\mathrm{T}}.
\end{aligned}
\tag{26}
$$

where the first four terms come from the isochoric part of Eq. (9) and the last two from the volumetric contribution. The linearization of the first Piola-Kirchhoff tensor of the Exponential model (Eq. (11))

is:

$$
\begin{aligned}
D_{\widehat{\boldsymbol{\eta}}}\mathrm{K}_{\mathsf{S}}(\mathbf{F}(\widehat{\boldsymbol{\eta}})) = \; & -\frac{2}{3}\alpha e^{\gamma(\mathrm{I}_1(\overline{\mathbf{C}})-3)}\mathrm{J}^{-2/3}(1+\gamma\mathrm{I}_1(\overline{\mathbf{C}}))(\mathbf{F}^{-\mathrm{T}}:\delta\mathbf{F})\mathbf{F}+ \\
& +\frac{2}{9}\alpha e^{\gamma(\mathrm{I}_1(\overline{\mathbf{C}})-3)}\mathrm{I}_1(\overline{\mathbf{C}})(1+\gamma\mathrm{I}_1(\overline{\mathbf{C}}))(\mathbf{F}^{-\mathrm{T}}:\delta\mathbf{F})\mathbf{F}^{-\mathrm{T}}+ \\
& -\frac{2}{3}\alpha e^{\gamma(\mathrm{I}_1(\overline{\mathbf{C}})-3)}\mathrm{J}^{-2/3}(1+\gamma\mathrm{I}_1(\overline{\mathbf{C}}))(\mathbf{F}:\delta\mathbf{F})\mathbf{F}^{-\mathrm{T}}+ \\
& +2\alpha e^{\gamma(\mathrm{I}_1(\overline{\mathbf{C}})-3)}\mathrm{J}^{-4/3}(\mathbf{F}:\delta\mathbf{F})\mathbf{F}+ \\
& +\alpha e^{\gamma(\mathrm{I}_1(\overline{\mathbf{C}})-3)}\mathrm{J}^{-2/3}\delta\mathbf{F}+ \\
& +\frac{2}{3}\alpha e^{\gamma(\mathrm{I}_1(\overline{\mathbf{C}})-3)}\mathrm{I}_1(\overline{\mathbf{C}})\mathbf{F}^{-\mathrm{T}}:\delta\mathbf{F}^{\mathrm{T}}\mathbf{F}^{-\mathrm{T}}+ \\
& +\frac{\kappa}{2}\mathrm{J}\Big(2\mathrm{J}-1+\frac{1}{J}\Big)(\mathbf{F}^{-\mathrm{T}}:\delta\mathbf{F})\mathbf{F}^{-\mathrm{T}}+ \\
& -\frac{\kappa}{2}(\mathrm{J}^2-\mathrm{J}+\mathrm{ln}\mathrm{J})\mathbf{F}^{-\mathrm{T}}\delta\mathbf{F}^{\mathrm{T}}\mathbf{F}^{-\mathrm{T}}.
\end{aligned}
\tag{27}
$$

where the first six terms represent the linearization of the isochoric part of Eq. (11). It is also possible to use an inexact Jacobian, saving part of the CPU-time required to compute the complete Jacobian. However, as it is well known, this approach can cause a reduction of the convergence rate of the Newton method.

Since the efficient solution of the nonlinearities is a key-point to save computational time and to obtain a second-order convergence rates of the Newton method in large structural problems (and for the physiological FSI simulations), particular attention has been devoted to the correct implementation of the Jacobian matrices defined above. In Sect. 4, validation test cases are run and the convergence rates of the Newton method in the case of pure structural dynamic problems are analyzed.

3.3. **Linearization of the FSI problem**

As shown in [25], when system (22) is discretized both in space and time and Newton iterations are performed, the tangent system has a block matrix, which contains on the diagonal the matrices of the single subproblems and in the off-diagonal postions the coupling terms. At each Newton iteration k the following correction step is obtained: *given* $\boldsymbol{u}_f^k$, $\widehat{\boldsymbol{\eta}}^k$, *and* $\boldsymbol{\eta}_f^k$, *find* $\delta\boldsymbol{u}_f^k$, $\delta\widehat{\boldsymbol{\eta}}^k$, *and* $\delta\boldsymbol{\eta}_f^k$ *such that*:

$$
\begin{bmatrix}
\mathcal{J}^k_{\mathsf{F}_{\boldsymbol{u}_f}} & \mathcal{J}^k_{\mathsf{F}_{\widehat{\boldsymbol{\eta}}}} & \mathcal{J}^k_{\mathsf{F}_{\boldsymbol{\eta}_f}} \\
0 & \mathcal{J}^k_{\mathsf{S}_{\widehat{\boldsymbol{\eta}}}} & \mathcal{J}^k_{\mathsf{S}_{\boldsymbol{\eta}_f}} \\
0 & \mathcal{J}^k_{\mathsf{G}_{\widehat{\boldsymbol{\eta}}}} & \mathcal{J}^k_{\mathsf{G}_{\boldsymbol{\eta}_f}}
\end{bmatrix}
\begin{Bmatrix}
\delta\mathbf{u}^k \\ \delta\widehat{\boldsymbol{\eta}}^k \\ \delta\boldsymbol{\eta}^k
\end{Bmatrix}
= -
\begin{Bmatrix}
\mathcal{R}_{\mathsf{F}}(\boldsymbol{u}_f,\widehat{\boldsymbol{\eta}},\boldsymbol{\eta}_f) \\
\mathcal{R}_{\mathsf{S}}(\boldsymbol{u}_f,\widehat{\boldsymbol{\eta}},\boldsymbol{\eta}_f) \\
\mathcal{R}_{\mathsf{H}}(\widehat{\boldsymbol{\eta}},\boldsymbol{\eta}_f)
\end{Bmatrix},
\tag{28}
$$

where the block $\mathcal{J}^k_{\mathsf{I}_j}$ is the Jacobian of the operator I with respect to the vector unknown j evaluated at the iteration k. The quantities $\mathcal{R}_{\mathsf{F}}$, $\mathcal{R}_{\mathsf{S}}$ and $\mathcal{R}_{\mathsf{H}}$ are the residuals of the fluid, structural and geometric problem respectively. When neglegting or approximating by finite differences the derivatives of the fluid and solid operators with respect to $\boldsymbol{\eta}_f$, the convergence of the Newton method can be very poor or even fail [22]. Hence, in this work we compute the exact Jacobian of the whole FSI problem, as it guarantees a second-order convergence.

	St. Venant-Kirchhoff	Neo-Hookean	Exponential
Newton r_0	8.32e+2	8.32e+2	8.32e+2
Newton r_1	1.87e+1	1.82e+1	1.82e+1
Newton r_2	1.60e-4	5.66e-5	7.31e-5
Newton r_3	2.20e-11	-	-
Convergence order d	3.07	3.32	3.25
Newton tolerance	8.35e-5	8.35e-5	8.35e-5
GMRES tolerance	1e-12	1e-12	1e-12

TABLE 1. Convergence properties of the Newton method for the nonlinear structural solver and related tolerences

4. Numerical Results

4.1. **Newton convergence test**

In order to check the correct implementation of the constitutive laws for the vessel wall (Eqs. (4)-(9)-(11)) and their Jacobians (Eqs. (25)-(26)-(27)) in `LifeV` , two different types of test cases have been carried out.

The first one is a pure structural dynamic test on a cube, while the second is an FSI test on a straight tube as in Fig. 1. Both types of problems are solved using the Newton method and the resulting algebraic linearized system is solved by the GMRES method. The stopping tolerance for the Newton method is defined as $\delta_{nonlin} = \delta_{abs} + \delta_{rel} * r_0$, where r_0 is the infinity norm of the first residual vector of the Newton method and δ_{abs} and δ_{rel} are the absolute and relative tolerances respectively. The order of convergence of the Newton method is defined as

$$d = \frac{log(\frac{r_2}{r_1})}{log(\frac{r_1}{r_0})} \tag{29}$$

where r_0, r_1, r_2 are the infinity norms of three consecutive residuals.
In the first test, an homogeneous Dirichlet boundary condition is imposed on one of the six faces of the geometry while a constant traction (equal to 10 mmHg) is applied on the opposite face to the Dirichlet side. On the remaining four faces, homogeneous Neumann conditions are applied. In Table 1, the convergence results obtained in the case of pure traction problem are shown. As expected, the order of convergence is never below the second order. In fact, from the theoretical point of view, the Newton method guarantees at least a second order convergence when the exact Jacobian is used in the computations.

In the case of the FSI test on a straight tube, the only non zero boundary condition has been imposed on the fluid domain. Referring to Fig. 1, a constant pressure equal to 10 mmHg has been applied at the inlet of the fluid domain while a homogeneous Neumann condition has been used at the outlet. Concerning the structure, the right and left extremities have been clamped and free stress have been applied on the outer wall. In Table 2 the decay of the infinity norm of the residual and the convergence rate of the Newton method of the FSI system are shown. Again, as expected, the Newton convergence rate is never below second order, since the exact Jacobian of the FSI problem has been used in the Newton method.

	St. Venant-Kirchhoff	Neo-Hookean	Exponential
Newton r_0	2.32e+3	2.32e+3	2.32e+3
Newton r_1	7.30e+1	2.89e+1	2.89e+1
Newton r_2	7.11e-3	3.60e-3	3.61e-3
Convergence order d	2.67	2.05	2.06
Newton tolerance	2.30e-1	2.30e-1	2.30e-1
GMRES tolerance	1e-12	1e-12	1e-12

TABLE 2. Convergence properties of the Newton method for the FSI test and related tolerances

E [dyn/cm^2]	ν[-]	μ [dyn/cm^2]	κ [dyn/cm^2]	α [dyn/cm^2]	γ [-]
$4 \cdot 10^6$	0.45	$1.38 \cdot 10^6$	$1.33 \cdot 10^7$	$1.38 \cdot 10^6$	1.00

TABLE 3. Structural parameters for aortic arch simulations

4.2. **Patient-specific FSI simulation in an aortic arch**

This section presents the numerical simulation of blood flow in the thoracic aorta. Different haemodynamic indicators, e.g. Wall Shear Stress (WSS), are compared using the different structural models considered above. Empirical evidence shows that the WSS distribution is responsible for the formation of pathologies such as the atherosclerosis [10], which is a severe and common disease and can lead to infarction and strokes. Knowing the pattern and the values for the WSS as output from a simulation can help the medical doctors in identifying critical regions and choosing a treatment.

The wall displacement and the consequent deformation of the arterial lumen is another useful information for physicians. In fact unphysiological deformations and eccentricity changes in the lumen can be indicators for pathologies and provide important information in the context of endovascular repairs [40]. Furthermore large differences in the displacements may modify as well the fluid dynamic and wall stresses.

The simulations have been run in parallel on 128 processors on the Cray XE6 supercomputer *Rosa* at the Swiss national supercomputing center CSCS. The physical parameters used for the simulation, resumed in Table 3, have been taken from literature, and correspond to a young healthy person. The fluid geometry is obtained with a manual segmentation from 3T-MRI data, while the structure has been extruded from the fluid-structure interface proportionally to the local radius. All these steps are detailed in [28] and numerical simulations obtained using this geometry and a linear elastic material are detailed in [5, 25, 29].

Both the fluid and solid problem have been discretized in time by a first order BDF method, with a time-step of $\delta t = 10^{-3}$ s. The equations have been discretized in space using P1–P1 interior penalty stabilized finite elements for the fluid problem, P1 for the structure and geometry problems. The linear system has been solved using GMRES, with tolerance (relative with respect to the first residual) $\delta_{lin} = 10^{-6}$. The relative tolerance for the Newton iterations is $\delta_{nonlin} = 10^{-3}$. The average number of iterations is approximately $2 - 3$ for all the models. The global Jacobian system solved at each Newton iteration consists of $5 \cdot 10^5$ degrees of freedom. The boundary conditions imposed at the fluid inlet-outlets are the flow rates obtained from a validated 1-D simulation on the same arterial tree [30]. For the structure a homogeneous Robin boundary condition has been imposed on the external wall simulating the presence of a surrounding tissue [5] with coefficient α between

$2 \cdot 10^4$ dyn/cm^3 (aorta) and $6 \cdot 10^4$ dyn/cm^3 (elsewhere). The boundary conditions for the structure outlets are of Neumann homogeneous type. At the structure outlets, homogeneous Neumann boundary conditions have been applied. This choice has been recently assessed in [24], where it has been shown not to produce significant numerical artifacts. The inlet boundary, in proximity of the aortic valve, is clamped. Below we compare the velocity and WSS fields (Figs. 4, 6, 7, 8), the radial displacement of the fluid interface (Fig. 2) obtained with the different models for the vessel wall and the wall displacement pattern (Fig. 3). In particular, Fig. 4 shows that, in the case of the exponential model, the velocity magnitude reaches higher values after the aortic arch and in the descending aorta. This corresponds to higher values of the WSS than the ones obtained with the linear elastic model in those regions of the domain (Figs. 7, 8). Fig. 2 highlights the differences in the radial displacement along the fluid-solid interface at the top of the aortic arch while Fig. 3 shows the wall displacement pattern. The three nonlinear models predict nearly the same radial displacement while the linear elastic law leads to higher values. This could imply an overestimation of the wall stresses and, consequently, to wrong predictions of the wall biological behaviour. In Fig. 8 the differences in the WSS distribution with respect to the one obtained using the linear elastic model are shown for each of the nonlinear laws. For the St. Venant-Kirchhoff material, the differences are mainly located in the left common carotid artery and on top of the aortic arch while in the rest of the domain they are negligible. In the case of the Neo-Hookean model, the differences on the WSS distribution are localized in the same region as for the St. Venant-Kirchhoff model while with the exponential model the WSS field shows non negligible differences in the descending thoracic aorta. Concerning the flow patterns at the peak systole, they are shown in Fig. 4. The predicted velocities are higher than those measured experimentally but the flow pattern (showed in Fig. 5) agrees with the experimental findings [7,8]. Indeed, at the late systole phase of the cardiac cycle, the helical secondary flow, which has been observed experimentally, is present. Fig. 6 shows the differences in the velocity magnitude at different heights of the fluid domain. As Fig. 8 confirms, the largest differences are obtained with the exponential model for the vessel wall.

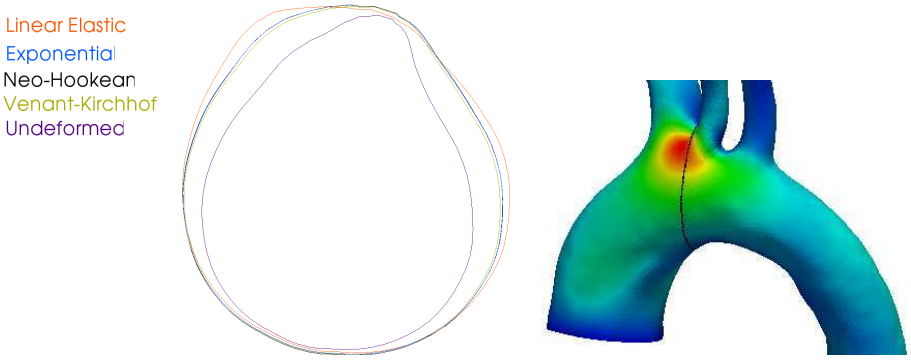

FIGURE 2. Representation of a section of the aortic arch at systole for the four different models.

(a) Linear elastic (b) St. Venant-Kirchhoff (c) Neo-Hookean (d) Exponential

FIGURE 3. Displacement pattern at the top of the aortic arch at $t = 0.2$ sec.

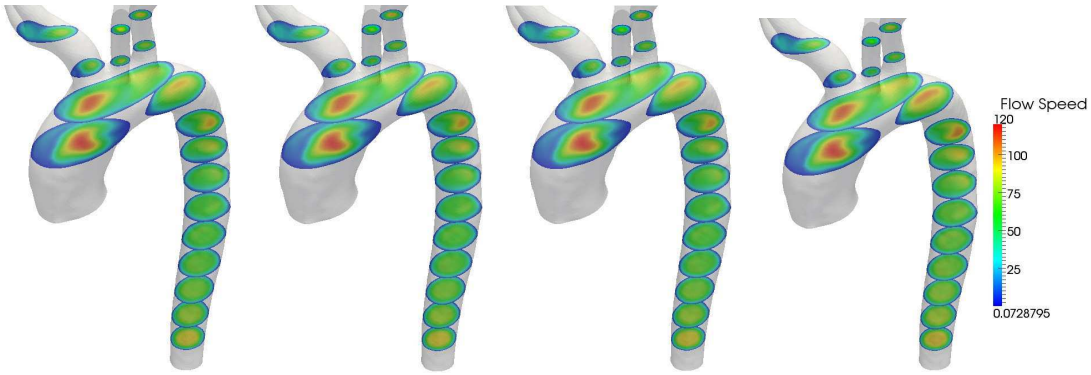

(a) Linear elastic (b) St. Venant-Kirchhoff (c) Neo-Hookean (d) Exponential

FIGURE 4. Velocity magnitude at different heights of the thoracic aorta at $t = 0.2$ sec.

5. Conclusions and perspectives

In this paper we have presented numerical fluid-structure simulations on a physisological geometry of aortic arch. In particular, we have focused our attention on four different constitutive laws for the arterial wall. In literature, hyperelastic isotropic constitutive laws frequently describe the mechanical properties of the vessel wall. In this paper, the arterial tissue has been modelled using the linear elastic, St. Venant-Kirchhoff, Neo-Hookean and exponential laws. As pointed out before, the coupled FSI problem is highly nonlinear due to the nonlinearity of both the structural and fluid problem. For this reason, no matter which technique is used to solve the FSI problem, their linearization is mandatory at each time step of the simulation. In the third section of the paper we have dedicated our attention to the linearization of the first Piola-Kichhoff tensor in the equation of motion to describe the vessel wall dynamics. We have detailed the expression of the Jacobian of the Piola-Kichhoff tensor for each nonlinear material model. As we have experimented, using the exact Jacobian is important in FSI simulations to reduce the computational time. The four structural models have been used in the context of physiological fluid-structure simulation on a aortic arch in order to understand the effects of the structural modeling on the solution.

As expected, when the arterial tissue is described by a nonlinear model, it behaves as a more rigid material than when it is modelled by the linear elastic case. This study show how some indicators such as WSS can be affected by the choice of the mechanical model for the wall. Even if those changes are not dramatic, they suggest that care must be taken in the choice of the structural model if an accurate indication is required.

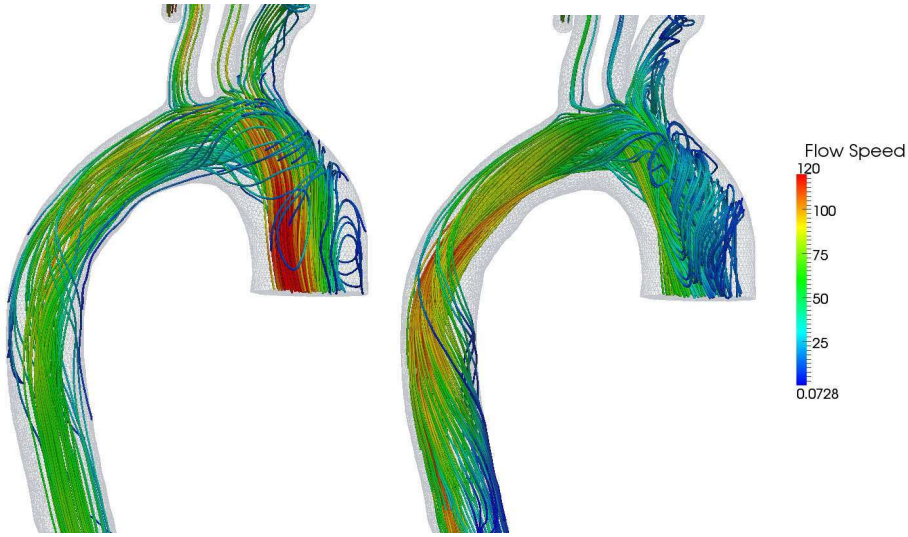

(a) Peak Systole (b) Late systole

FIGURE 5. Stream lines in the fluid domain at peak systole ($t = 0.2$ sec) and late systole ($t = 0.3$ sec)

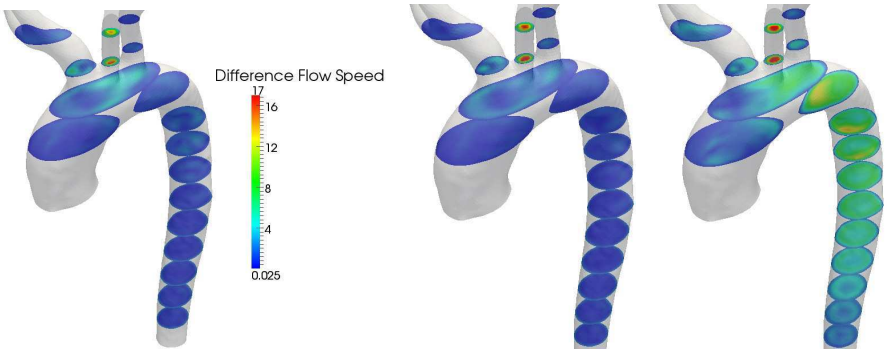

(a) St. Venant-Kirchhoff (b) Neo-Hookean (c) Exponential

FIGURE 6. Differences in the velocity field magnitude at different heights of the thoracic aorta at systole ($t = 0.2$ sec).

The mathematical description of the biological evolution of the tissues (e.g. growth and remodelling) is an open field of research. It is known that the arterial tissue responds to haemodynamics stimula it receives (e.g. in the context of endovascular repairs) and for this reason, it is important to evaluate how different haemodynamics indicators, e.g. the WSS distribution and velocity field change when the structural law changes.

Clearly this work is still preliminary. We need to assess the effect of anisotropy and pre-stress of the arterial tissue, topics that will be investigated in future works.

An important issue in these simulations is also the availability of reliable geometric data. Yet, the rapid evolution of medical imaging devices let us believe that accurate geometry reconstructions

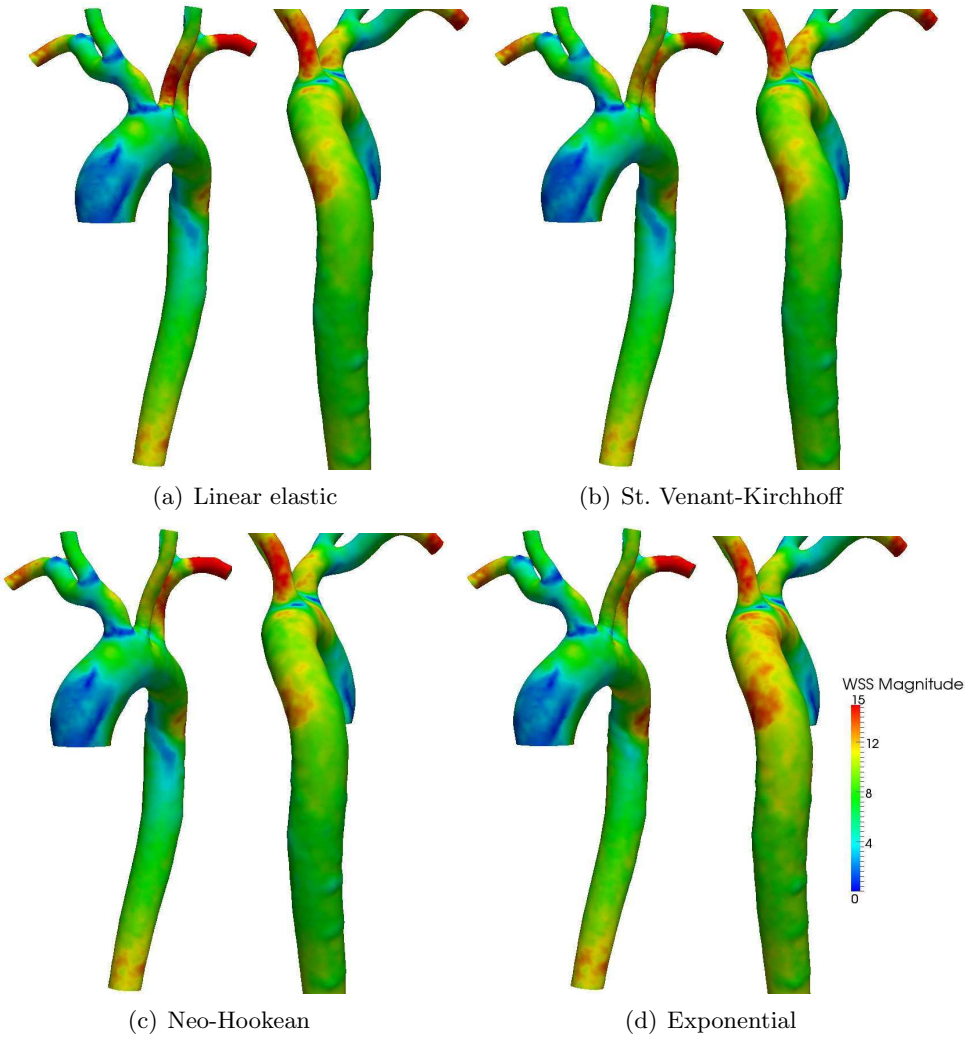

(a) Linear elastic (b) St. Venant-Kirchhoff

(c) Neo-Hookean (d) Exponential

FIGURE 7. WSS for the four models at systole ($t = 0.2$ sec).

will be commonly available in the near future, as well as accurate data about flow rate. This makes the importance of investigating reliable methods for the simulation of blood flow in patient specific geometries even more paramount.

REFERENCES

1. Crosetto P. Deparis S. Fourestey G. Quarteroni A., *Parallel Algorithms for Fluid-Structure Interaction Problems in Haemodynamics*, Siam Journal of Scientific Computing **33** (2011), no. 4, 1598–1622.
2. Raoult A., *Non Policonvexity of the Stored Energy Function of a St. Venant-Kirchhoff Material*, Aplikace Matematiki **6** (1986), 417–419.
3. Nixon A. M. Gunel M. Sumpio B.E., *The Critical Role of Hemodynamics in the Development of Cerebral Vascular Disease*, Journal of Neurosurgery **112** (2010), 1240–1253.
4. Cebral J.R. Mut F. Weir J. Putman C.M., *Association of Hemodynamic Characteristics and Cerebral Aneurysm Rupture*, American Journal of Neuroradiology **32** (2011), no. 2, 264–270.

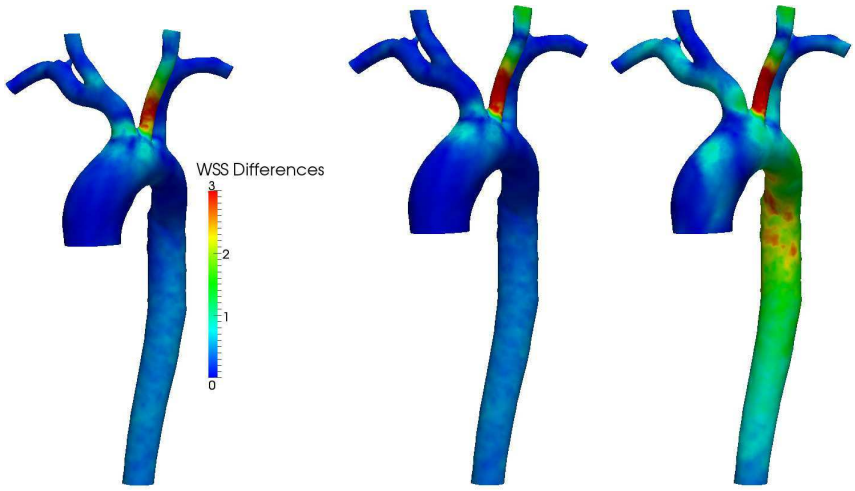

(a) St. Venant-Kirchhoff (b) Neo-Hookean (c) Exponential

FIGURE 8. Difference between the WSS ($^{\text{Dyn}}/_{\text{cm}^2}$) computed with the linear elastic and the other three models at systole.

5. Paolo Crosetto, Philippe Reymond, Simone Deparis, Dimitrios Kontaxakis, Nikolaos Stergiopulos, and Alfio Quarteroni, *Fluid-structure interaction simulation of aortic blood flow*, Computers & Fluids **43** (2011), no. 1, 46–57.
6. Zakaria H. Robertson A.M. Kerber C.W., *A Parametric Model for Studies of Flow in Arterial Bifurcations*, Annals of Biomedical Engineering **36** (2008), no. 9, 1515–1530.
7. Killner PJ. Yang GZ. Mohiaddin RH. Firmin DN. Lonfmore DB., *Helical and Retrograde Secondary Flow Pattern in the Aortic Arch Studied by Three-Directional Magnetic Resonance Velocity Mapping*, Journal of the American Heart Association **88** (1993), 2235–2247.
8. _____, *Two Dimensional Flow Quantitative MRI of Aortic Arch Blood Flow Patterns: Effects of Age, Sex, and Presence of Carotid Atheromatous Disease on Prevalence of Spiral Blood Flow*, Journal of Magnetic Resonance Imaging **18** (2003), 169–174.
9. École Polytechnique Fédérale de Lausanne (CMCS), CH; Politecnico di Milano (MOX), ITA; INRIA (REO, ESTIME), FR, and Emory University (Math&CS), GA US., *Lifev*, 2010, LifeV user manual, `http://lifev.org`.
10. Formaggia L. Quarteroni A. Veneziani A. (Eds), *Cardiovascular Mathematics. Modeling and Simulation of the Circulatory System*, MS & A, vol. 1, Springer, 2009.
11. Valencia A. Solis F., *Blood Flow Dynamics and Arterial Wall Interaction in a Saccular Aneurysm Model of the Basilar Artery*, Computers & Structures **84** (2006), 1326–1337.
12. Ciarlet P. G., *Mathematical elasticity*, vol. I, Elsevier, 1988.
13. Holzapfel G.A., *Nonlinear solid mechanics: A continuum approach for engineering*, Wiley, 2000.
14. Schulze-Bauer C.A.J. Regitinig P. Holzapfel G.A., *Mechanics of the Human Femoral Adventitia Including High-Pressure Response*, American Journal of Physiology - Heart Circulation Physiology **282** (2002), 2427–2440.
15. Humphrey J.D., *Cardiovascular Solid Mechanics*, Springer, 2002.
16. _____, *Continuum Biomechanics of Soft Biological Tissue*, Proceedings of the Royal Society A **459** (2002), 3–46.
17. Bazilev Y. Hsu M.C. Zhang Y. Wang W. Kvamsdal T. Hentschel S. Isaksen J.G., *Computational Vascular Fluid-Structure Interaction: Methodology and Application to Cerebral Aneurysms*, Biomechanics and Modeling in Mechanobiology **9** (2010), 481–498.
18. Bazilev Y. Hsu M.C. Zhang Y. Wang W. Liang X. Kvamsdal T. Brekken R. Isaksen J.G., *A Fully-Coupled Fluid-Structure Interaction Simulation of Cerebral Aneurysms*, Computational Mechanics **46** (2010), 3–16.
19. Ottesen J.T. Olufsen M.S. Larsen J.K., *Applied Mathematical Models in Hman Physiology*, Society for Industrial and Applied Mathematics, 2004.
20. Sforza D.M. Putman C.M. Cebral J.R., *Hemodynamics of Cerebral Aneurysms*, Annual Review of Fluid Mechanics **41** (2009), 91–107.

21. Deluca M., *Mathematical and numerical models for cerebral aneurysms wall mechanics*, Ph.D. thesis, Politecnico di Milano, 2009.
22. Fernandez M.A. Moubachir M., *A Newton Method using Exact Jacobians for Solving Fluid-Structure Coupling*, Computers & Structures **83** (2005), 127–142.
23. Robertson S. Sequeira A. Kameneva M., *Hemorheology*, in Galdi G.P. Rannacher R. Robertson A. Turek S. (Eds), Haemodynamical Flows: Modelling Analysis and Simulation, Oberwolach Seminars, vol. 37, pp. 63–120, Birkhauser, 2008.
24. A. C. I. Malossi, P. J. Blanco, P. Crosetto, S. Deparis, and A. Quarteroni, *Implicit coupling of one-dimensional and three-dimensional blood-flow models with compliant vessels*, Submitted, 2011.
25. Crosetto P., *Fluid-Structure Interaction Problems in Hemodynamics: Parallel Solvers, Preconditioners, and Applications*, Ph.D. thesis, École Polytechinque Fédérale de Lausanne, 2011.
26. Humphrey J.D. Canham P.B., *Structure, Mechanical Properties, and Mechanics of Intracranial Saccular Aneurysms*, Journal of Elasticity **61** (2000), 49–81.
27. Bonet J Wood R.D., *Nonlinear continuum mechanics for finite element analysis*, Cambridge University Press, 1997.
28. P. Reymond, Y. Bohraus, F. Perren, F. Lazeyras, and N. Stergiopulos, *Validation of a person specific 1-d model of the systemic arterial tree*, XII Mediterranean Conference on Medical and Biological Engineering and Computing 2010 (R. Magjarevic, J. H. Nagel, Panagiotis D. Bamidis, and Nicolas Pallikarakis, eds.), IFMBE Proceedings, vol. 29, Springer Berlin Heidelberg, 2010, pp. 578–579.
29. Philippe Reymond, Paolo Crosetto, Simone Deparis, Alfio Quarteroni, and Nikos Stergiopulos, *Physiological aspects of fluid structure interaction and their effects on blood flow in a person-specific aorta.*, Submitted, 2011.
30. Philippe Reymond, Fabrice Merenda, Fabienne Perren, Daniel Rufenacht, and Nikos Stergiopulos, *Validation of a one-dimensional model of the systemic arterial tree*, Am J Physiol Heart Circ Physiol **297** (2009), no. 1, H208–222.
31. Foutrakis G.N. Yonas H. Sclabassi R.J., *Saccular Aneurysm Formation in Curved and Bifurcating Arteries*, American Journal of Neuroradiology **20** (1999), 1309–1317.
32. Holzapfel G.A. Odgen R.W., *Constitutive Modeling of Arteries*, Proceedings of the Royal Society A **466** (2010), 1551–1597.
33. Ogden R.W., *Nonlinear elastic deformations*, vol. II, Dover, 1997.
34. Malek A. Alper S. Izumo S., *Hemodynamics Shear Stress and Its Role in Atherosclerosis*, Journal of the American Medical Association **282** (1999), no. 21, 2035–2042.
35. Wick T., *Fluid-Structure Interactions using Different Mesh Motion Techniques*, Computer & Structures **89** (2011), 1456–1467.
36. Holzapfel G.A. Gasser T.C., *A New Constitutive Framework for Arterial Wall Mechanics and a Comparative Study of Material Models*, Journal of Elasticity **61** (2000), 1–48.
37. Torii R. Oshima M. Kobayashi T. Takagi K. Tezduyar T.E., *Fluid-Structure Interaction Modeling of a Patient-Specific Cerebral Aneurysm: Influence of Structural Modeling*, Computational Mechanics **43** (2008), 151–159.
38. ———, *Influencing Factors in Image-Based Fluid-Structure Interaction Computation of Cerebral Aneurysms*, International Journal for Numerical Methods in Fluids **65** (2011), 324–340.
39. Bazilev Y. Calo V.M. Zhang Y. Hughes T.J.R., *Isogeometric FluidStructure Interaction Analysis with Applications to Arterial Blood Flow*, Computational Mechanics **38** (2006), 310–322.
40. J. van Prehn, K.L. Vincken, S.M. Sprinkhuizen, M.A. Viergever, J.W. van Keulen, J.A. van Herwaarden, F.L. Moll, and L.W. Bartels, *Aortic pulsatile distention in young healthy volunteers is asymmetric: Analysis with ecg-gated mri*, European Journal of Vascular and Endovascular Surgery **37** (2009), no. 2, 168 – 174.
41. Fung Y.C., *Biomechanics*, Springer, 1993.
42. Xie J. Zhou J. Fung Y.C., *Bending of Blood Vessel Wall: Stress-Strain Laws of the Intima-Media and Adventitia Layers*, Journal of Biomechanical Engineering **117** (1995), 136–145.

MOX Technical Reports, last issues

Dipartimento di Matematica "F. Brioschi",
Politecnico di Milano, Via Bonardi 9 - 20133 Milano (Italy)

15/2012 Mengaldo, G.; Tricerri, P.; Crosetto,P.; Deparis, S.; Nobile, F.; Formaggia, L.
A comparative study of different nonlinear hyperelastic isotropic arterial wall models in patient-specific vascular flow simulations in the aortic arch

14/2012 Fumagalli, A.;Scotti, A.
An unfitted method for two-phase flow in fractured porous media.

13/2012 Formaggia, L.; Guadagnini, A.; Imperiali, I.; Lever, V.; Porta, G.; Riva, M.; Scotti, A.; Tamellini, L.
Global Sensitivity Analysis through Polynomial Chaos Expansion of a basin-scale geochemical compaction model

12/2012 Guglielmi, A.; Ieva, F.; Paganoni, A.M.; Ruggeri, F.
Hospital clustering in the treatment of acute myocardial infarction patients via a Bayesian semiparametric approach

11/2012 Bonnemain, J.; Faggiano, E.; Quarteroni A.; Deparis S.
A Patient-Specific Framework for the Analysis of the Haemodynamics in Patients with Ventricular Assist Device

10/2012 Lassila, T.; Manzoni, A.; Quarteroni, A.; Rozza, G.
Boundary control and shape optimization for the robust design of bypass anastomoses under uncertainty

09/2012 Mauri, L.; Perotto, S.; Veneziani, A.
Adaptive geometrical multiscale modeling for hydrodynamic problems

08/2012 Sangalli, L.M.; Ramsay, J.O.; Ramsay, T.O.
Spatial Spline Regression Models

07/2012 Perotto, S; Zilio, A.
Hierarchical model reduction: three different approaches

06/2012 Micheletti, S.; Perotto, S.
Anisotropic recovery-based a posteriori error estimators for advection-diffusion-reaction problems